Núñez Valdez, M., Efthimiopoulos, I., Taran, M., Müller, J., Bykova, E., McCammon, C., Koch-Müller, M., Wilke, M. (2018): Evidence for a pressure-induced spin transition in olivine-type LiFePO4 triphylite. - *Physical Review B*, *97*, 18.

DOI: http://doi.org/10.1103/PhysRevB.97.184405

Evidence for a pressure-induced spin transition in olivine-type $LiFePO_4$ triphylite

Maribel Núñez Valdez,[1,*] Ilias Efthimiopoulos,[1,2,†] Michail Taran,[1,3] Jan Müller,[1,4] Elena Bykova,[5] Catherine McCammon,[6] Monika Koch-Müller,[1] and Max Wilke[2]

[1]*GFZ German Research Centre for Geosciences, Telegrafenberg, 14473 Potsdam, Germany*
[2]*Institute of Earth and Environmental Science, University of Potsdam, Karl-Liebknecht-Strasse 24-25, 14476 Potsdam-Golm, Germany*
[3]*National Academy of Sciences of Ukraine, Institute of Geochemical Mineral and Ore Format, UA-03680 Kiev 142, Ukraine*
[4]*Institute of Geology and Mineralogy, University of Cologne, Zulpicher Strasse 49b, 50674 Cologne, Germany*
[5]*FS-PE, PETRA III, Deutsches Elektronen Synchrotron, 22607 Hamburg, Germany*
[6]*Bayerisches Geoinstitut, Universität Bayreuth, 95440 Bayreuth, Germany*

(Received 17 January 2018; revised manuscript received 13 April 2018; published 3 May 2018)

We present a combination of first-principles and experimental results regarding the structural and magnetic properties of olivine-type $LiFePO_4$ under pressure. Our investigations indicate that the starting $Pbnm$ phase of $LiFePO_4$ persists up to 70 GPa. Further compression leads to an isostructural transition in the pressure range of 70–75 GPa, inconsistent with a former theoretical study. Considering our first-principles prediction for a high-spin to low-spin transition of Fe^{2+} close to 72 GPa, we attribute the experimentally observed isostructural transition to a change in the spin state of Fe^{2+} in $LiFePO_4$. Compared to relevant Fe-bearing minerals, $LiFePO_4$ exhibits the largest onset pressure for a pressure-induced spin state transition.

DOI: 10.1103/PhysRevB.97.184405

I. INTRODUCTION

Compounds belonging to the lithiophilite-triphylite series $LiM2PO_4$ where $M2$ represents a metal ($M2$ = Mn,Fe) are commonly found throughout the Earth's crust and mantle in pegmatites with high Li and P content [1,2]. At ambient conditions, they are isostructural with $(Mg,Fe)_2SiO_4$-olivine [space-group (SG) 62, $Pbnm$ and $Z = 4$], one of the most abundant minerals (∼50–60% vol) in the upper mantle of our planet (<410-km depth and pressure of $P < 13.5$ GPa) [3]. Figure 1 shows this olivine-type structure, which can be seen as a distorted hexagonal close packing of oxygen anions with corner-sharing $M2O_6$ and edge-sharing LiO_6 octahedra aligned in parallel chains along the **b** axis. The P ions are in PO_4 tetrahedra linking the octahedral layers.

The transition-metal $M2$ in these $LiM2(PO_4)$ phosphate materials is octahedrally coordinated (Fig. 1), which leads to the crystal-field splitting (Δ) of the $M2$ $3d$ electrons into three lower-energy levels t_{2g} and two higher-energy levels e_g. At low pressures, Hund's rule predicts that, for example, $M2 = Fe^{2+}$ (ferrous iron) adopts the high-spin (HS) state with $S = 2$ ($t_{2g}^4 e_g^2$). However, as pressure increases, Δ increases at the expense of the spin-pairing exchange energy J ($J < \Delta$), and Fe^{2+} undergoes a spin transition to the energetically more favorable low-spin (LS) state with $S = 0$ ($t_{2g}^6 e_g^0$). Using computational and experimental (EXP) approaches, this pressure-induced spin crossover has been investigated and reported in several Fe-bearing minerals of the Earth's lower mantle (in the range of 660–2890-km depth and 23–135 GPa), such as (Mg,Fe)O-ferropericlase [4–17], $(Mg,Fe)SiO_3$-bridgmanite [18–25], and $(Mg,Fe)CO_3$-magnesiosiderite [26–36]. The study of this HS-to-LS transition is important as it has effects on the structural, optical, elastic, and thermodynamic properties of the Fe-bearing host minerals and in consequence potential and profound geophysical repercussions in the interpretation of seismic velocities and geodynamical modeling [12,16,37]. In addition to the aforementioned minerals, it was reported using density functional theory (DFT) [39,40] that $LiFePO_4$-triphylite also undergoes a HS-to-LS spin crossover at about 52 GPa although not in the $Pbnm$ structure but rather as a $Cmcm$ high-pressure (HP) and high-temperature (HT) phase, which was shown to become the ground state at ∼4 GPa [41]. Experimentally, the $Pbnm \rightarrow Cmcm$ structural transformation was observed at 6.5 GPa and 1173 K [42]. Recently, however, some controversy regarding the validity of the structural and spin transitions has emerged as recent experimental and computational studies addressing the structural stability of $LiFePO_4$ under pressure [43,44] have shown that the $Pbnm$ phase is stable up to ∼30 GPa. Thus, leaving somewhat open and unresolved the issues of whether or not: (1) the $Pbnm \rightarrow Cmcm$ structural phase transition occurs in triphylite at room temperature (RT), and if not, (2) does the $Pbnm$ phase undergo a HS-to-LS transition similar to other Fe-bearing minerals [4,18,26]?

Aside from the geophysical relevance of these $LiM2PO_4$ olivine-type materials, in recent years, $LiFePO_4$-triphylite has also attracted considerable interest as a storage cathode material in rechargeable Li batteries (for a review see, e.g., Ref. [45] and references therein). For example, Li^+ migration depends on the compressibility and structural symmetry of $LiFePO_4$-triphylite [44]. Hence, a thorough study of triphylite will allow us to better understand the properties of this material and its potential high-pressure applications.

*mari_nv@gfz-potsdam.de
†iliefthi@gfz-potsdam.de

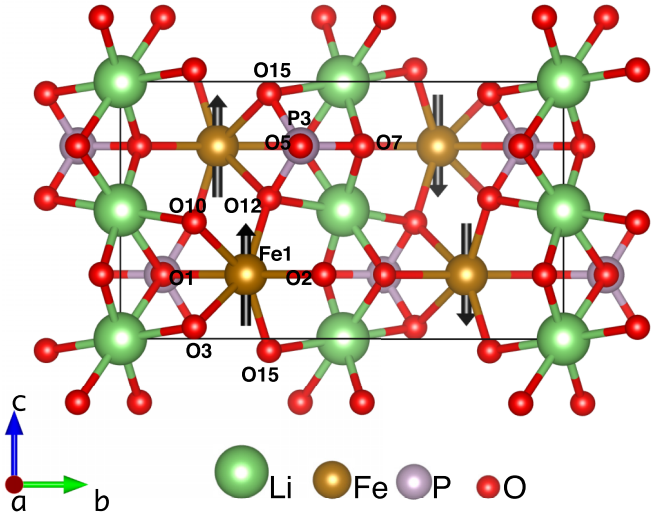

(a)

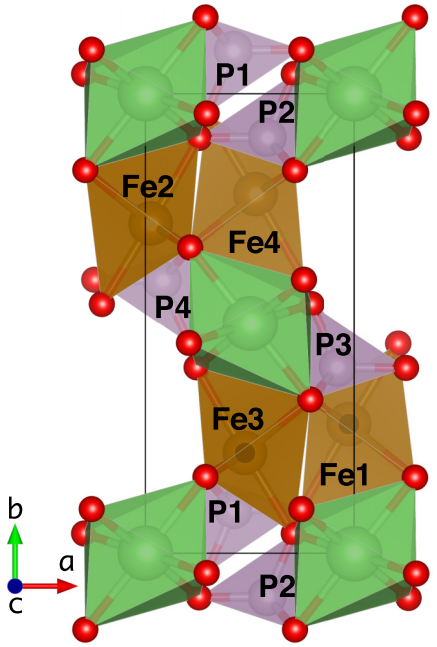

(b)

FIG. 1. At ambient pressure, $LiFePO_4$-triphylite ($M2$ = Fe) crystallizes in the olivine-type structure (SG 62, $Pbnm$, $Z = 4$) with antiferromagnetic (AFM) ordering. Selected Fe, P, and O atoms are indicated for later analysis in Sec. IV. (Crystal structures in this paper are visualized using VESTA [38].) (a) The ground state of $Pbnm$ $LiFePO_4$. The AFM ordering is indicated with the black arrows. (b) Polyhedral representation of $LiFePO_4$.

Partly motivated by a possible pressure-induced HS → LS transition in $LiFePO_4$, we have expanded the investigated high-pressure structural and vibrational behaviors of triphylite up to 80 GPa at RT by means of synchrotron-based x-ray diffraction (XRD), infrared (IR), and Raman spectroscopies. Additionally, we have performed *ab initio* calculations to investigate the structural stability of $LiFePO_4$-triphylite under pressure and the potential spin crossover in the energetically most favorable phase. By comparing the experimentally determined volume as a function of pressure to the theoretical trends throughout the pressure range considered (0–90 GPa), we provide evidence for a pressure-induced HS-to-LS transition in the $Pbnm$-$LiFePO_4$ phase. After presenting our experimental (Sec. II A) and computational methods (Sec. II B), we give comprehensive results concerning the experimental determination of vibrational and structural parameters (Secs. III A and III B) and computational structural and enthalpy trends (Sec. III C) as a function of pressure. We then discuss the spin crossover in $LiFePO_4$ (Sec. IV) and finally present our conclusions (Sec. V). Characterization of samples, additional figures, and tables with more experimental measurements and computational results can be found in the Supplemental Material [46].

II. METHODS

A. Experimental details

We have investigated two synthetic $LiFePO_4$ samples: The first one was commercial powder (Sigma-Aldrich 97% purity, sample A), and the second sample was micrometer-sized single crystals (sample B) synthesized by combined high-pressure and high-temperature treatments of the aforementioned $LiFePO_4$ powder in the multi-anvil press installed at GeoForschungsZentrum (GFZ) [47] as follows (MA502): Sample A was enclosed in a Pt capsule, whereas the 18/11 assembly was used. Pressure was raised to 1.4 GPa, then temperature was raised to 1373 K (melting), and the sample remained there for 30 min. Within 2 h, the temperature was slowly decreased down to 973 K. The multi-anvil press was rotated for 2 h at this temperature. Throughout the whole experiment, the pressure was kept at 1.4 GPa.

The characterization of sample A by means of XRD and Raman spectroscopy at ambient conditions revealed the presence of two additional impurity phases at an ∼30% concentration (as estimated by the relative Bragg-peak intensities), i.e., the rhombohedral and monoclinic modifications of $Li_3Fe_2(PO_4)_3$, both of them being Fe^{3+} bearing and common during the preparation of $LiFePO_4$ [48]. In addition, Mössbauer spectroscopy evidenced a 30% content of Fe^{3+} for sample A, in excellent agreement with our XRD measurements. On the other hand, the characterization of sample B was performed with XRD, electron microprobe analysis (EMPA), energy loss spectroscopy (EELS), and Raman and Mössbauer spectroscopies. For the EMPA measurements, several crystals of the recovered sample MA502 were selected, mounted in epoxy, polished, and coated with carbon for EMPA using a JEOL Hyperprobe JXA-8500F EMP with a field-emission cathode. As standard materials for Mg and Si, we used a natural olivine, and for Fe and P, we used hematite and Durango apatite, respectively. The analytical conditions included an acceleration voltage of 15 kV, a beam current of 20 nA, and a beam diameter of 1 μm. The Li_2O content was calculated as the difference to 100%. In order to check for any traces of Fe^{3+} in the synthesized single crystals, Mössbauer experiments were conducted on almost 100 crystals piled together on plastic with clear nail varnish and covering 400 microns in diameter. Data collection took 13 days. Finally, the presence of ferric iron in the synthetic single crystals was additionally checked with EELS. We cut a thin foil from a

polished single crystal from the aforementioned microprobe mount using a FEI focused ion-beam 200 device. EELS were collected with a FEI Tecnai G2 F20 X-Twin TEM operating at 200 kV with a field-emission gun electron source and a Gatan Trideim energy filter with an energy resolution of 1 eV. Details of the measurements and interpretation can be found in Ref. [49]. The combined EMPA, EELS, and Mössbauer measurements yield the following chemical composition for sample B: $(Li_{0.94}, Fe^{3+}_{0.06})(Fe^{2+}_{0.79}, Mg_{0.18})PO_4$. More information on the characterization of the starting $LiFePO_4$ samples A and B is provided in the Supplemental Material [46].

Gasketed diamond-anvil cells (DACs) equipped with low-fluorescence type-II diamonds of 250- and 200-μm culet diameters were used for pressure generation. The rhenium gaskets were preindented to ∼25-μm thicknesses with holes of 100-μm diameters acting as sample chambers in separate runs. Argon served as the pressure-transmitting medium (PTM) in all spectroscopic experiments, whereas neon was used for the XRD measurements. The ruby-fluorescence method was employed for pressure calibration [50].

The high-pressure mid-IR (MIR) measurements at RT were conducted on $LiFePO_4$ powder pressed into a thin film (sample A) with the Vertex 80v Fourier-transform IR spectrometer coupled to a Hyperion 2000 microscope at GFZ within the 500–1800-cm^{-1} spectral range. We used a KBr beam splitter and a Hg-Cd-Te detector. The spectra were averaged over 512 scans with a spectral resolution of 2 cm^{-1}. For details of the thin-film preparation for IR experiments, see, e.g., Ref. [51].

Our high-pressure RT Raman measurements were conducted with a Horiba Jobin Yvon LabRam HR800 VIS spectrometer at GFZ, equipped with a blue ($\lambda = 473$-nm) solid-state laser operating at a power of 2 mW outside the DAC. The same $LiFePO_4$ thin film measured with MIR (sample A) as well as single crystals of sample B with typical dimensions of 40×40 μm^2 were measured within the 100–1200-cm^{-1} frequency region.

The angle-resolved high-pressure XRD measurements were performed at the Extreme Conditions Beamline P02.2 of PETRA III (Hamburg, Germany) [52] with an incident x-ray wavelength of $\lambda = 0.289$ Å and a beam size of 2×2 μm^2. Two-dimensional XRD patterns were collected with a fast flat panel detector XRD1621 from PerkinElmer (2048 pixels × 2048 pixels, 200 × 200-pixel size) and processed with the FIT2D software [53]. Refinements were performed using the GSAS + EXPGUI software packages [54]. Due to the presence of impurities in sample A as we discussed earlier, we investigated only sample B with XRD by crushing the small single crystals into powder between the diamonds of the DAC.

B. Computational details

The computational results presented in our paper were obtained by applying DFT [39,40] within the projector-augmented plane-wave (PAW) [55,56] method as implemented in the VASP (version 5.4.4) software [56–58] installed in the supercomputer JURECA [59]. We employed primarily the general-gradient approximation (GGA) in the Perdew-Burke-Ernzerhof (PBE) [60] prescription for the exchange-correlation potential, and for comparison we also tested the local-density approximation (LDA) [61]. The default PAW potentials with

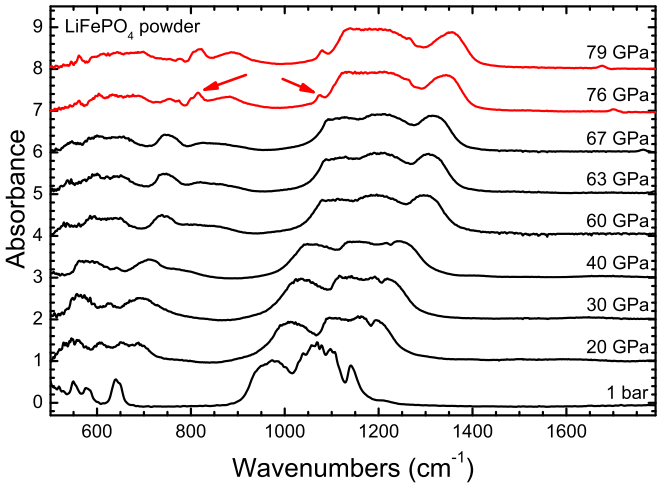

FIG. 2. MIR spectra of $LiFePO_4$ sample A at various pressures. The black and red spectra correspond to the *Pbnm* and the HP-*Pbnm* phases, respectively. The red arrows indicate the new MIR bands (see the text).

the valence configurations of $1s^2 2s^1$ for lithium, $3p^6 3d^7 4s^1$ for iron, $3s^2 3p^3$ for phosphorous, and $2s^2 2p^4$ for oxygen were used throughout our calculations. We adopted a plane-wave kinetic-energy cutoff of 500 eV and a uniform Γ-centered grid with $(2\pi \times 0.032)$-$Å^{-1}$ spacing for the reciprocal space sampling of our 28-atom cells for pressures between −5 and 100 GPa. The Hubbard-U correction [62,63] was added to the localized Fe $3d$ electrons (LDA + U and PBE + U), and we assessed its value in the range of 0–5.3 eV but found $U = 2.5$ eV to better agree with the experimentally determined lattice parameters and the pressure at which evidence of a spin transition is observed in $LiFePO_4$ (see Figs. 5 and 6 in the Supplemental Material [46]). Convergence of our calculations at each pressure was assumed when the forces on each atom were smaller than 1 meV/Å and the total energy changes less than 10^{-8} eV. Triphylite structures were set up at each target pressure within the *Pbnm* and *Cmcm* space groups and subsequently fully relaxed (internal coordinates and lattice parameters) using a conjugate gradient minimization approach. At zero pressure, the ordering of the spin of Fe^{2+}, i.e., AFM and ferromagnetic (FM) configurations, was also probed.

III. RESULTS

A. Vibrational spectroscopy under pressure

According to group theory [64–66], the expected IR- and Raman-active modes in $LiFePO_4$ are as follows:

$$\Gamma = 11A_g + 11B_{1g} + 7B_{2g} + 7B_{3g} + 14B_{1u} + 14B_{2u} + 10B_{3u}. \quad (1)$$

Thus, $LiFePO_4$ has 36 Raman-active modes ($11A_g + 11B_{1g} + 7B_{2g} + 7B_{3g}$) and 38 IR-active modes ($14B_{1u} + 14B_{2u} + 10B_{3u}$). In Fig. 2, we present selected high-pressure MIR spectra collected for sample A. The ambient-pressure MIR spectrum of $LiFePO_4$ is consistent with the reported literature [67,68]. The intense broad MIR bands located between 1000 and 1200 cm^{-1} correspond to internal antisymmetric

TABLE I. Volume V, bulk modulus B, its pressure derivative B' for $Pbnm$ $LiFePO_4$, and its HP-$Pbnm$ phase as obtained by a Birch-Murnaghan EoS [70] fitted to our measured and computed P-V data $^\diamond$. "Fixed" values were not allowed to vary during the fitting. Other results are from *: Ref. [71]; †: Ref. [44]; ‡: Ref. [43].

$LiFePO_4$ phase	Method	P (GPa)	V (Å^3)	B (GPa)	B' (GPa)
$Pbnm$	EXP$^\diamond$	0.0	290.80 (fixed)	99.0(1)	4.0 (fixed)
	GGA + $U^\diamond$	0.0	299.00	90.9	4.3
	GGA + $U^\star$	0.0	299.54	94.7	
	EXP†	0.0	292.38	91.5	4.0 (fixed)
	GGA + $U^\dagger$	0.0	292.38	92.9	
	LDA + $U^\dagger$	0.0	300.62	114.1	
	EXP‡	0.0	291.60	106.0(8)	
HP-$Pbnm$	EXP$^\diamond$	73.0	203.00 (fixed)	545.0(2)	4.0 (fixed)
HP-$Pbnm$ (LS)	GGA + $U^\diamond$	73.0	196.47	381.0	4.0

P-O stretching vibrations ν_3, the broadband centered at ~960 cm^{-1} belongs to the symmetric P-O stretching motion ν_1, and the IR region between 400 and 800 cm^{-1} is mainly attributed to the internal bending motions of the PO_4 tetrahedra ν_2 and ν_4 [64,67,68]. The complete assignment can be found in Table I in the Supplemental Material [46].

Increasing pressure leads to the frequency upshift and a broadening of the recorded MIR bands, owing partly to the nonhydrostatic conditions imposed by the Ar PTM upon increasing pressure [69] as well as the polycrystalline form of our sample. Nevertheless, close to 70 GPa we can detect the appearance of new IR bands between 700 and 800 cm^{-1} and at 1000 cm^{-1}, indicating a pressure-induced transition of the $Pbnm$-$LiFePO_4$ structure. We will identify this high-pressure modification as HP-$Pbnm$ from now on. Interestingly, we can observe that the broadband at 750 cm^{-1} is apparently vanishing in the new phase with no other significant changes taking place throughout the transition.

Concurrently with our MIR experiment, we performed Raman spectroscopic investigations on the same $LiFePO_4$ thin film (sample A). Selected Raman spectra at various pressures are shown in Fig. 3(a). We note that the strongest Raman peak located at 950 cm^{-1} corresponds to the symmetric P-O ν_1 stretching vibration [64,66]. Increasing pressure leads to the appearance of a small shoulder in the vicinity of the aforementioned ν_1 mode at 67 GPa, indicating the phase transition of $LiFePO_4$ towards HP-$Pbnm$ at this pressure and in excellent agreement with our MIR results. Further compression results in the intensity enhancement of this shoulder at the expense of the 950-cm^{-1} peak. Moreover, we can observe the

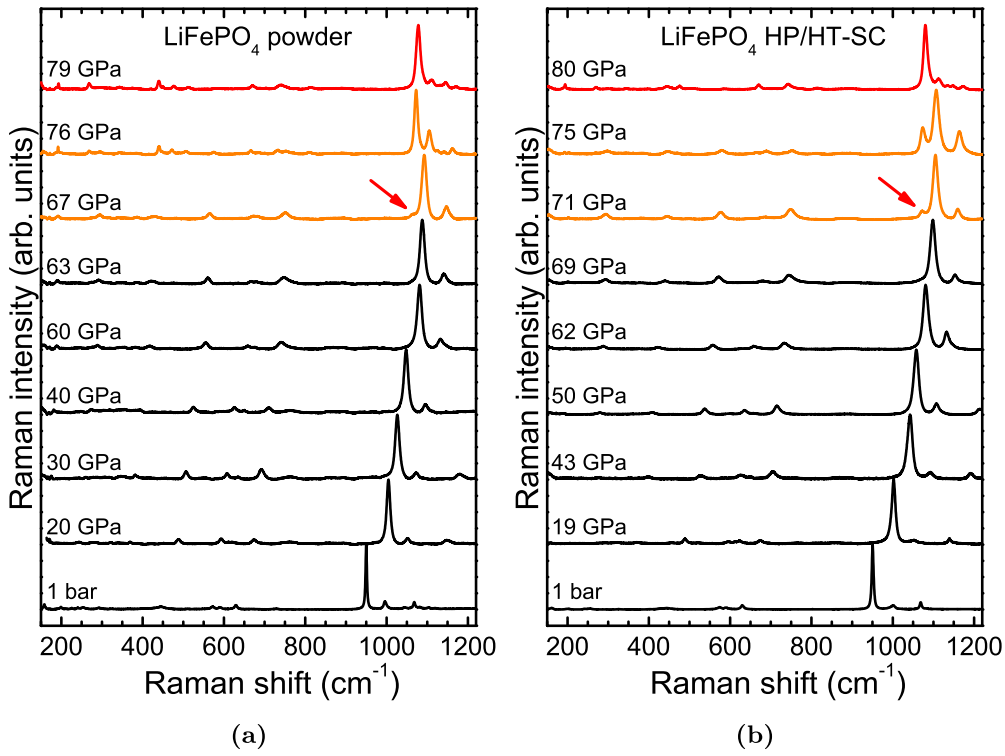

FIG. 3. Raman spectra of $LiFePO_4$ (a) sample A and (b) sample B at selected pressures. The black, red, and orange spectra correspond to the $Pbnm$, the HP-$Pbnm$ phases, and the coexistence range, respectively. The red arrows indicate the new Raman features in both cases (see the text).

appearance of several low-intensity Raman features (Fig. 4 in the Supplemental Material [46]).

In order to test whether this pressure-induced transition is possibly a by-product of the polycrystalline nature of our sample or its impurities (see the Supplemental Material [46]), we have additionally conducted high-pressure Raman investigations on the (HP/HT)-synthesized $LiFePO_4$ single crystals. The relevant Raman spectra are plotted in Fig. 3(b). As we can observe clearly, the situation is identical with that of sample A, i.e., a new Raman peak in the vicinity of the strong 950-cm^{-1} mode emerges at 71 GPa. We note that the Raman spectra at ∼80 GPa for both samples are practically identical, indicating that the pressure-induced $Pbnm \rightarrow$ HP-$Pbnm$ structural transition of $LiFePO_4$ is inherent to the material and independent of the starting condition of the sample. At this stage, we cannot assign the high-pressure modification to the predicted nonmagnetic $Cmcm$ phase (calculated to be adopted close to 52 GPa) [41] as its Raman spectrum has not been reported.

B. Structure under pressure

Following our vibrational spectroscopic results, we have additionally conducted high-pressure XRD experiments in order to identify the aforementioned phase transition close to 70 GPa. We have only probed the structural behavior of sample B since the Bragg peaks of the impurities in sample A (see Sec. II A as well as the Supplemental Material [46]) might hinder the clear detection of a structural change. Overall, the XRD patterns collected up to 79 GPa reveal indeed a transition initiating at 69 GPa as exposed by the appearance of a shoulder in the Bragg peak centered at $2\theta \simeq 7^\circ$ [Fig. 4(a)]. Further compression leads to the enhancement of this shoulder at the expense of the 7° Bragg peak attributed to the starting $Pbnm$ phase.

Indexing of the XRD pattern at 78.5 GPa is possible again with a $Pbnm$ structure [Fig. 4(b)]. Hence, $LiFePO_4$ undergoes an isostructural transition close to 70 GPa; the transition pressure lies in excellent agreement with our vibrational studies discussed above. According to our extracted lattice parameters, in Fig. 5(a), upon passing from the $Pbnm$ to the HP-$Pbnm$ phase, the orthorhombic **b** axis decreases by ∼3%, which in turn results in an overall volume reduction of ∼3% (Fig. 5). Thus, the isostructural $Pbnm \rightarrow$ HP-$Pbnm$ transition can be classified as of first order. We should also note that we tested the proposed $Cmcm$ phase [41], but it could not reproduce the observed high-pressure XRD patterns.

In Fig. 5 we plot the measured pressure-volume (P-V) data alongside the respective EoS fittings and our GGA+U (with $U = 2.5$-eV) results. The extracted elastic parameters are listed in Table I. As we can observe, our volume at zero pressure V_0 and bulk modulus B_0 values for the starting $Pbnm$ phase of $LiFePO_4$ are in good agreement with the reported literature [43,44,71].

C. Structural relaxations

In order to complement and verify our experimental results, we also performed DFT calculations. For this purpose, first we stabilized the AFM and FM configurations of $Pbnm$

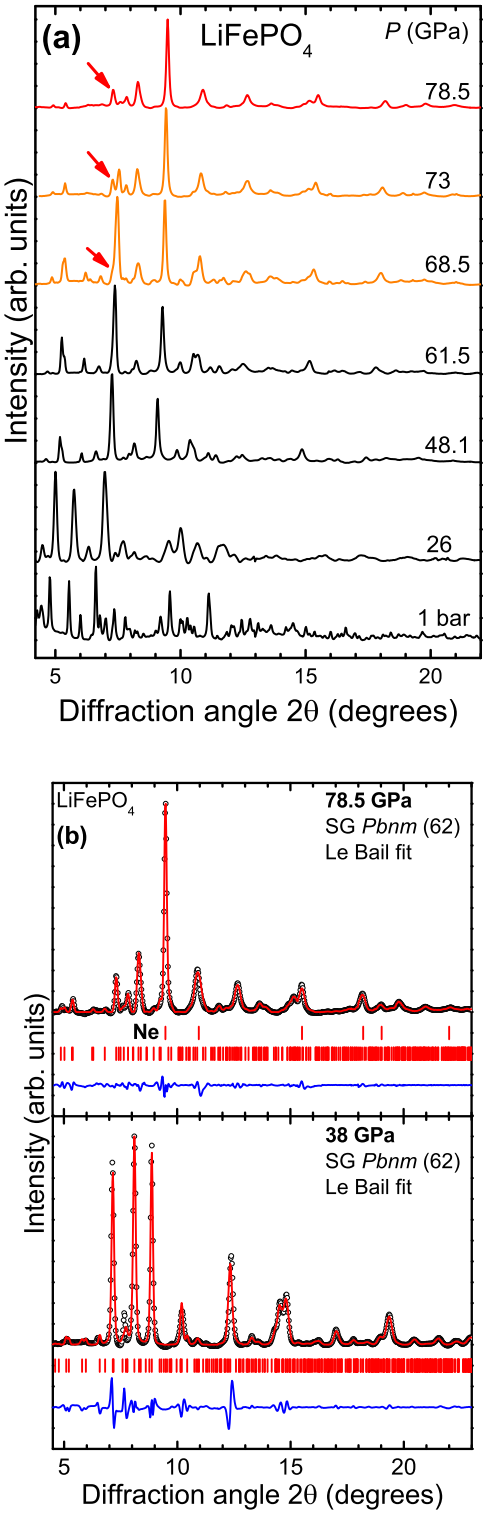

FIG. 4. (a) Selected XRD patterns of $LiFePO_4$ (sample B) at various pressures ($T = 300$ K, $\lambda = 0.29$ Å). The $Pbnm$ phase is shown in black, the HP-$Pbnm$ phase is shown in red, and their coexistence range is depicted in orange. The red arrows indicate the new XRD features (see the text). (b) Examples of Le Bail refinements at 38 GPa (bottom) and 78.5 GPa (top). The black circles and the red solid lines correspond to the measured and the fitted patterns, whereas their difference is depicted as a blue line. The vertical ticks mark the Bragg-peak positions for the $Pbnm$ phase and the neon PTM (only the top).

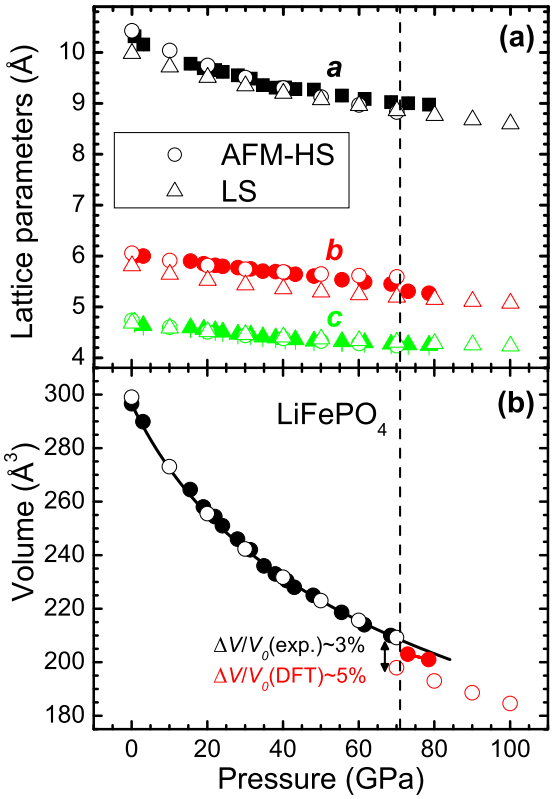

FIG. 5. (a) Lattice parameters (EXP: the solid symbols; DFT + U: the open symbols) and (b) unit-cell volume as a function of pressure for $Pbnm$ $LiFePO_4$ ($\lesssim$73 GPa; EXP: the solid black circles; DFT + U: the open black circles) and its HP-$Pbnm$ phase ($\gtrsim$73 GPa; EXP: the solid red circles; DFT + U: the open red circles). The solid lines running through the symbols are the fitted Birch-Murnaghan equation of state (EoS) forms. The vertical dashed line marks the onset of the isostructural transition. Error bars lie within the symbols.

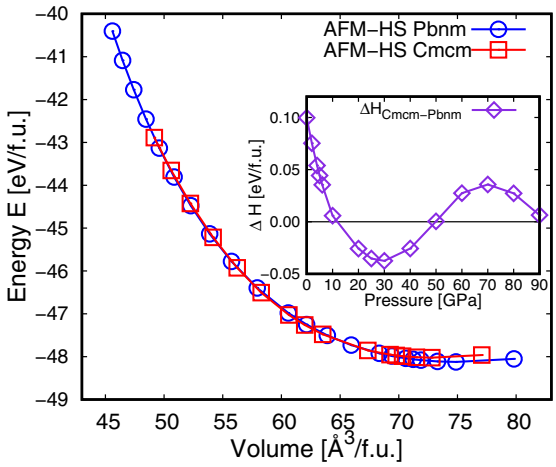

FIG. 6. Calculated total internal energy per f.u. as a function of volume per f.u. for the two AFM structures of $LiFePO_4$ considered, $Pbnm$ and $Cmcm$. The inset: Stability of these phases as shown by their relative enthalpies as a function of pressure.

and $Cmcm$ $LiFePO_4$ at ambient pressure and determined the AFM ordering of $Pbnm$ $LiFePO_4$ to be the ground state at ~7.5 and ~12.5 meV per formula unit (f.u.) lower than the FM $Pbnm$ $LiFePO_4$ and the AFM $Cmcm$ $LiFePO_4$ for $U = 4.3$ eV, respectively. We began with $U = 4.3$ eV as this value was used in the most recent work on the stability of triphylite [44], and although U seems to be not considered by Lin and Zeng [41] in their $Pbnm \rightarrow Cmcm$ phase-transition study, the authors also report AFM ordering as the ground states for their $Pbnm$- and $Cmcm$-triphylite phases. We note that AFM $Pbnm$ $LiFePO_4$ holds as the ground state independent of U (= 0,2.5,3.3,4.3,5.3 eV). The energy differences we found are consistent with first-principles calculations also performed in $LiFePO_4$ as part of a study of Li compounds [72] at ambient conditions. Thus, in the rest of the paper we only examine AFM phases with $U = 2.5$ eV as it was the value to produce the most compatible structural parameters and description of the high-pressure spin state of $LiFePO_4$ (Fig. 5).

Our static DFT results for the total internal energy (E) per f.u. as a function of volume per f.u. of the AFM $Pbnm$- and $Cmcm$-triphylite phases are shown in Fig. 6. As one can see, the equations of state of these two phases are nearly identical for high pressures. To further assess the stability of the orthorhombic $Pbnm$-$LiFePO_4$ phase with respect to $Cmcm$ $LiFePO_4$, we calculated their enthalpy (H) as a function of pressure (P), volume (V), and internal energy (E) at each P,

$$H(P) = E[V(P)] + PV(P). \quad (2)$$

We found, that as pressure increases, as shown in the inset of Fig. 6, the difference in enthalpy per f.u. (ΔH) between the $Pbnm$ and the $Cmcm$ phases fluctuates for $P > 10$ GPa, i.e., -0.04 eV $< \Delta H < 0.04$ eV, making these two competing phases almost degenerate within the accuracy of our static first-principles method. However, upon comparison with the structural XRD refinements [Fig. 4(a)], the $Pbnm$ structure is favored in this pressure range. Therefore, we conclude that the proposed pressure-induced $Pbnm \rightarrow Cmcm$ phase transition in $LiFePO_4$ [41] is not likely at RT. Further examination contrasting our experimental and calculated lattice parameters of $LiFePO_4$-triphylite shows, in general, an excellent agreement for the starting AFM-HS $Pbnm$ phase ($\lesssim$75 GPa), Fig. 5(a) (see also Fig. 5 and Tables III–V in the Supplemental Material [46]). Upon reaching the transition pressure point, we notice that the magnitude of the lattice parameter along the **b** axis undergoes the largest decrease thus contributing greatly to the volume drop (Fig. 5) observed experimentally (~3%) and predicted by GGA + U (~5%). We should note here that the modest agreement between the experimental and the calculated volume reductions across the HS-to-LS transition in $LiFePO_4$ can be partially attributed to the sensitive nature of the DFT + U method. In particular, it has been established that the choice of U can significantly affect both the spin transition pressure as well as the volume difference between the two phases. For example, in the case of $FeCO_3$, within the GGA + U approximation, $U = 0$ eV results in a transition pressure of 15 GPa and a volume reduction of 12.5%, whereas $U = 4$ eV shifts the transition pressure to 28 GPa and the volume difference to ~10% [73]; furthermore, using a self-consistent U parameter (GGA + U) gives a transition pressure range of 47–50 GPa and a volume drop of ~10% at the transition point [34]. These results, still contrast, to

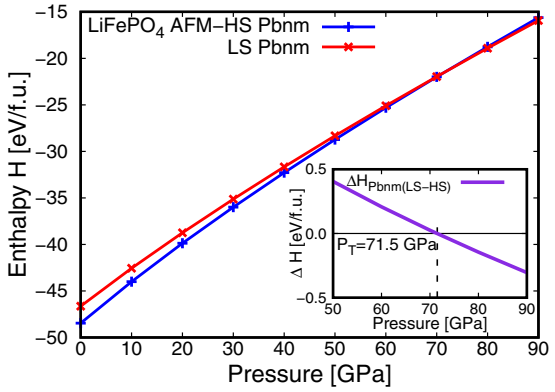

FIG. 7. Enthalpy of *Pbnm* $LiFePO_4$ in HS and LS states as a function of pressure. The inset shows the spin transition pressure (P_T) as predicted from GGA + U with $U = 2.5$ eV.

a varying degree, the experiments on $FeCO_3$, which exhibit transition pressures within the 43–52-GPa pressure range, and the corresponding volume reductions varying between 6.5% and 10% [28–30]. In our case, if we choose GGA + U with $U = 4.3$ eV (see Figs. 5 and 6 in the Supplemental Material [46]), we obtain a volume reduction of 4%, which is in much better agreement with the collapsed volume observed in our experiments of ∼3%, but this outcome is at the cost of an increase in the HS → LS transition pressure with respect to the one experimentally determined. Additionally, we also have to consider that our DFT computations were performed at 0 K, whereas the experiment was performed at room temperature. Given also the fact that the chemical composition of our experimental single-crystalline sample is not stoichiometric $LiFePO_4$ as in our calculations but rather a slightly more complicated chemical formula, i.e., $(Li_{0.94}, Fe^{3+}_{0.06})(Fe^{2+}_{0.79}, Mg_{0.18})PO_4$, we can expect differences in the exact volume reduction at the HS-to-LS transition point, similar to the $(Fe_x, Mg_{1-x})CO_3$ solid solution series [30].

IV. SPIN TRANSITION

As we have already mentioned in Sec. I, high-pressure studies of Fe-bearing minerals have established a HS-LS transition upon sufficient compression [4,18,26]. This magnetic change is usually accompanied by a first-order isostructural transition, i.e., the crystalline symmetry is retained during the HS-LS transition, whereas the first-order character is attributed to the reduction of the Fe^{2+} ionic radius upon the spin change [74]. Using DFT we studied the spin state behavior of *Pbnm* $LiFePO_4$ as a function of pressure within GGA + U with $U = 2.5$ eV. We stabilized *Pbnm* $LiFePO_4$ in its LS state and computed its enthalpy [Eq. (2)] to compare it to that of *Pbnm* $LiFePO_4$ in the AFM-HS configuration for pressures between 0 and 90 GPa. Figure 7 shows the switch in spin state from HS to LS at about 72 GPa, in excellent agreement with the observed transition pressure in our experiments. To further corroborate the presence of this spin crossover, we also investigated the relative enthalpies of the HS and LS states using other U values within the GGA + U and LDA + U schemes. Our results, detailed in our Supplemental Material [46], indicate that the spin transition occurs for all values of U tested (Fig. 5 in the Supplemental Material [46]) and that the spin transition pressure predicted by GGA + U increases with U. LDA + U also showed this spin crossover, however, the structural parameters and volume of triphylite computed within this scheme were grossly underestimated (see Fig. 6 in the Supplemental Material [46]).

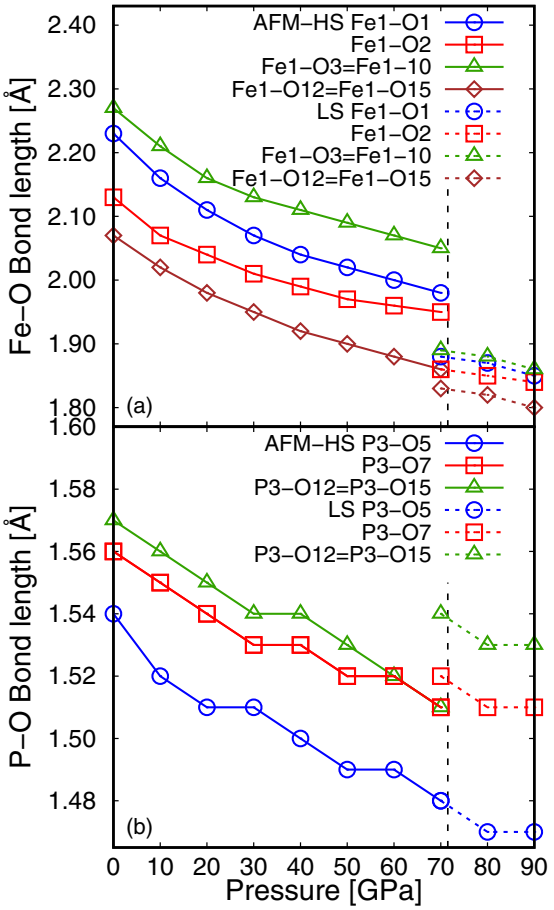

FIG. 8. Computed (a) Fe1-O and (b) P3-O bond length distances as a function of pressure for *Pbnm* $LiFePO_4$ in HS and LS states within GGA + U with $U = 2.5$ eV. The vertical dashed lines mark the onset of the isostructural transition. Bond lengths for Fe2-O, Fe3-O, Fe4-O, P1-O, P2-O, and P3-O are analogous (see Fig. 1).

In order to gain a microscopic structural understanding of the HS-to-LS transition in $LiFePO_4$, we plot selected *ab initio* Fe-O and P-O bond lengths as a function of pressure (Fig. 8). As we can clearly observe in Fig. 8(a), all the Fe-O bond distances shrink abruptly at the transition point, following the decrease in the Fe^{2+} ionic radius upon the spin crossover. This effect has been previously observed in other Fe-bearing compounds [27,28,37]. At the same time, we note that three of the P-O bonds increase across the transition pressure, Fig. 8(b). This P-O bond enlargement lies in excellent agreement with our Raman investigations where a frequency downshift of the ν_1 mode was observed at the transition point (Fig. 3). Since the ν_1 mode corresponds to the symmetric P-O stretching motion [64,67], its frequency downshift implies an increase in the associated P-O bonds at the spin crossover. Our DFT + U calculations have indeed captured this effect.

Considering the very good consistency between our experimental and computational results, we can establish at this point that $LiFePO_4$ undergoes a *spin-driven* isostructural transition at ∼70 GPa with its magnetic configuration changing from AFM to nonmagnetic owing to the pressure-induced HS-LS transition. Compared to relevant Fe-bearing minerals [4–34,36], $LiFePO_4$ exhibits the highest onset pressure for a spin transition to date. A plausible explanation might be the incompressibility of the FeO_6 octahedra in the olivine structure compared to, e.g., the ferropericlase and carbonate structures. In Fig. 8 we can see that as pressure increases, the Fe-O bond-length distance first decreases rather rapidly but at about 40 GPa, the contraction rate decreases.

Finally, we would like to add some thoughts on the possible effect of the HS-to-LS transition on the $LiFePO_4$ performance as a cathode material, i.e., on the Li^+ diffusion properties. The effect of pressure on the Li^+ diffusion rate has been modeled up to 28 GPa [44]. These calculations showed that the Li^+ migration barrier energy doubles along each possible diffusion direction, i.e., the volume reduction hinders the Li^+ diffusion and, consequently, diminishes the $LiFePO_4$ battery performance. Furthermore, we can reasonably assume that a potential pressure-induced Fe^{2+} spin transition might reduce the $LiFePO_4$ cathode efficiency even further, following the smaller unit-cell volume of the LS configuration compared to the HS state as a result of the Fe^{2+} ionic radius reduction. Another preventive factor might be the empty Fe^{2+} e_g states of the LS state; such a conclusion was reached for perovskite oxides [75]. On the other hand, the symmetrization of the Fe-O bond lengths upon the HS-to-LS transition (Fig. 8) may enhance the Li^+ mobility in LS-$LiFePO_4$, partially counteracting the aforementioned hindering factors of battery efficiency and performance in this particular material [76].

V. CONCLUSIONS

We have investigated the olivine-type $LiFePO_4$ structural and magnetic properties under pressure with a combination of first-principles and experimental probes. Our investigations indicate that the starting *Pbnm* phase of $LiFePO_4$ persists up to ∼70 GPa. Further compression leads to a first-order isostructural transition in the pressure range of ∼70–75 GPa, inconsistent with previous claims regarding the adoption of a *Cmcm* structure at ∼4 GPa [41]. Considering our DFT results placing a high-spin-to-low-spin transition of Fe^{2+} close to 72 GPa, we attribute the experimentally observed isostructural transition to a change in the spin state of Fe^{2+} in $LiFePO_4$, i.e., a transition from the starting AFM-*Pbnm* phase towards a nonmagnetic state. To date, our results imply that $LiFePO_4$ exhibits the highest onset pressure for a spin state transition among Fe-bearing minerals, resulting most likely from the larger incompressibility of its FeO_6 octahedra.

ACKNOWLEDGMENTS

We thank Dr. R. Wirth for his assistance with the EELS measurements. This work was supported by the Deutsche Forschungs Gemeinschaft (DFG) Funds No. Ko1260/18 and No. Wi2000/10. Parts of this research were carried out at the light source PETRA III at DESY, a member of the Helmholtz Association (HGF). M.N.V. gratefully acknowledges the computing time granted by the John von Neumann Institute for Computing (NIC) and provided on the supercomputer JURECA at Jülich Supercomputing Centre (JSC) under Project No. ID HPO24. Some computations were also performed at the GFZ linux cluster GLIC.

[1] A. Losey, J. Rakovan, J. M. Hughes, C. A. Francis, and M. D. Dyar, Can. Mineral. **42**, 1105 (2004).
[2] K. Langer, M. N. Taran, and A.-M. Fransolet, Eur. J. Mineral. **18**, 337 (2006).
[3] A. E. Ringwood, *Composition and Petrology of the Earth's Mantle* (McGraw-Hill, New York, 1975), p. 618.
[4] J. Badro, Science **300**, 789 (2003).
[5] J.-F. Lin, V. V. Struzhkin, S. D. Jacobsen, M. Y. Hu, P. Chow, J. Kung, H. Liu, H.-k. Mao, and R. J. Hemley, Nature (London) **436**, 377 (2005).
[6] S. Speziale, A. Milner, V. E. Lee, S. M. Clark, M. P. Pasternak, and R. Jeanloz, Proc. Natl. Acad. Sci. USA **102**, 17918 (2005).
[7] T. Tsuchiya, R. M. Wentzcovitch, C. R. S. da Silva, and S. de Gironcoli, Phys. Rev. Lett. **96**, 198501 (2006).
[8] A. F. Goncharov, V. V. Struzhkin, and S. D. Jacobsen, Science **312**, 1205 (2006).
[9] J.-F. Lin, G. Vanko, S. D. Jacobsen, V. Iota, V. V. Struzhkin, V. B. Prakapenka, A. Kuznetsov, and C.-S. Yoo, Science **317**, 1740 (2007).
[10] J. C. Crowhurst, J. M. Brown, A. F. Goncharov, and S. D. Jacobsen, Science **319**, 451 (2008).
[11] R. M. Wentzcovitch, J. F. Justo, Z. Wu, C. R. S. da Silva, D. A. Yuen, and D. Kohlstedt, Proc. Natl. Acad. Sci. USA **106**, 8447 (2009).
[12] H. Marquardt, S. Speziale, H. J. Reichmann, D. J. Frost, F. R. Schilling, and E. J. Garnero, Science **324**, 224 (2009).
[13] D. Antonangeli, J. Siebert, C. M. Aracne, D. L. Farber, A. Bosak, M. Hoesch, M. Krisch, F. J. Ryerson, G. Fiquet, and J. Badro, Science **331**, 64 (2011).
[14] Z. Wu, J. F. Justo, and R. M. Wentzcovitch, Phys. Rev. Lett. **110**, 228501 (2013).
[15] E. Holmström and L. Stixrude, Phys. Rev. Lett. **114**, 117202 (2015).
[16] Z. Wu and R. M. Wentzcovitch, Proc. Natl. Acad. Sci. USA **111**, 10468 (2014).
[17] H. Hsu, K. Umemoto, Z. Wu, and R. M. Wentzcovitch, Rev. Mineral. Geochem. **71**, 169 (2010).
[18] J. Badro, Science **305**, 383 (2004).
[19] J. Li, V. V. Struzhkin, H.-K. Mao, J. Shu, R. J. Hemley, Y. Fei, B. Mysen, P. Dera, V. Prakapenka, and G. Shen, Proc. Natl. Acad. Sci. USA **101**, 14027 (2004).
[20] C. McCammon, I. Kantor, O. Narygina, J. Rouquette, U. Ponkratz, I. Sergueev, M. Mezouar, V. Prakapenka, and L. Dubrovinsky, Nat. Geosci. **1**, 684 (2008).

[21] J.-F. Lin, H. Watson, G. Vankó, E. E. Alp, V. B. Prakapenka, P. Dera, V. V. Struzhkin, A. Kubo, J. Zhao, C. McCammon, and W. J. Evans, Nat. Geosci. **1**, 688 (2008).

[22] H. Hsu, K. Umemoto, P. Blaha, and R. M. Wentzcovitch, Earth Planet. Sci. Lett. **294**, 19 (2010).

[23] H. Hsu, P. Blaha, M. Cococcioni, and R. M. Wentzcovitch, Phys. Rev. Lett. **106**, 118501 (2011).

[24] V. Potapkin, C. McCammon, K. Glazyrin, A. Kantor, I. Kupenko, C. Prescher, R. Sinmyo, G. V. Smirnov, A. I. Chumakov, R. Rüffer, and L. Dubrovinsky, Nat. Commun. **4**, 1427 (2013).

[25] H. Hsu and R. M. Wentzcovitch, Phys. Rev. B **90**, 195205 (2014).

[26] A. Mattila and T. Pylkkänen, J. Phys.: Condens. Matter **19**, 386206 (2007).

[27] B. Lavina, P. Dera, R. T. Downs, V. Prakapenka, M. Rivers, S. Sutton, and M. Nicol, Geophys. Res. Lett. **36**, 2 (2009).

[28] B. Lavina, P. Dera, R. T. Downs, W. Yang, S. Sinogeikin, Y. Meng, G. Shen, and D. Schiferl, Phys. Rev. B **82**, 064110 (2010).

[29] T. Nagai, T. Ishido, Y. Seto, D. Nishio-Hamane, N. Sata, and K. Fujino, J. Phys.: Conf. Ser. **215**, 012002 (2010).

[30] G. Farfan, S. Wang, H. Ma, R. Caracas, and W. L. Mao, Am. Mineral. **97**, 1421 (2012).

[31] J. F. Lin, J. Liu, C. Jacobs, and V. B. Prakapenka, Am. Mineral. **97**, 583 (2012).

[32] J. Liu, J.-F. Lin, Z. Mao, and V. B. Prakapenka, Am. Mineral **99**, 84 (2014).

[33] S. S. Lobanov, A. F. Goncharov, and K. D. Litasov, Am. Mineral. **100**, 1059 (2015).

[34] H. Hsu and S. C. Huang, Phys. Rev. B **94**, 060404 (2016).

[35] J. Müller, S. Speziale, I. Efthimiopoulos, S. A. Jahn, and M. Koch-Müller, Am. Mineral. **101**, 2638 (2016).

[36] J. Müller, I. Efthimiopoulos, S. A. Jahn, and M. Koch-Müller, Eur. J. Mineral. **29**, 785 (2017).

[37] J.-F. Lin, S. Speziale, Z. Mao, and H. Marquardt, Rev. Geophys. **51**, 244 (2013).

[38] K. Momma and F. Izumi, J. Appl. Cryst. **41**, 653 (2008).

[39] P. Hohenberg and W. Kohn, Phys. Rev. **136**, B864 (1964).

[40] W. Kohn and L. J. Sham, Phys. Rev. **140**, A1133 (1964).

[41] H. Lin and Z. Zeng, IEEE Trans. Magn. **47**, 3817 (2011).

[42] O. García-Moreno, M. Alvarez-Vega, F. García-Alvarado, J. García-Jaca, J. M. Gallardo-Amores, M. L. Sanjuán, and U. Amador, Chem. Mater. **13**, 1570 (2001).

[43] J. L. Dodd, *Phase Composition and Dynamical Studies of Lithium Iron Phosphate*, Ph.D. thesis, California Institute of Technology, Pasadena, CA, 2007.

[44] H. Dong, H. Guo, Y. He, J. Gao, W. Han, X. Lu, S. Yan, K. Yang, H. Li, D. Chen, and H. Li, Solid State Ionics **301**, 133 (2017).

[45] J. Wang and X. Sun, Energy Environ. Sci. **8**, 1110 (2015).

[46] See Supplemental Material at http://link.aps.org/supplemental/10.1103/PhysRevB.97.184405 for more information on the characterization of $LiFePO_4$ samples and detailed structural experimental and computational results.

[47] M. Koch-Müller, E. Mugnaioli, D. Rhede, S. Speziale, U. Kolb, and R. Wirth, Am. Mineral. **99**, 2405 (2009).

[48] C. M. Julien, K. Zaghib, A. Mauger, and H. Groult, Adv. Chem. Eng. Sci. **2**, 321 (2012).

[49] M. Mrosko, M. Koch-Müller, C. McCammon, D. Rhede, J. R. Smyth, and R. Wirth, Contrib. Mineral. Petrol. **170**, 9 (2015).

[50] K. Syassen, High Press. Res. **28**, 75 (2008).

[51] M. Mrosko, M. Koch-Müller, and U. Schade, Am. Mineral. **96**, 1748 (2011).

[52] H.-P. Liermann, Z. Konopkova, W. Morgenroth, K. Glazyrin, J. Bednarcik, E. E. McBride, S. Petitgirard, J. T. Delitz, M. Wendt, Y. Bican, A. Ehnes, I. Schwark, A. Rothkirch, M. Tischer, J. Heuer, H. Schulte-Schrepping, T. Kracht, and H. Franz, J. Synchrotron Radiat. **22**, 908 (2015).

[53] A. P. Hammersley, S. O. Svensson, M. Hanfland, A. N. Fitch, and D. Hausermann, High Press. Res. **14**, 235 (1996).

[54] B. H. Toby, J. Appl. Crystallogr. **34**, 210 (2001).

[55] P. E. Blöchl, Phys. Rev. B **50**, 17953 (1994).

[56] G. Kresse and D. Joubert, Phys. Rev. B **59**, 1758 (1999).

[57] G. Kresse and J. Furthmüller, Comput. Mater. Sci. **6**, 15 (1996).

[58] G. Kresse and J. Furthmüller, Phys. Rev. B **54**, 11169 (1996).

[59] Jülich Supercomputing Centre, J. Large-Scale Res. Facilities **2**, A62 (2016).

[60] J. P. Perdew, K. Burke, and M. Ernzerhof, Phys. Rev. Lett. **77**, 3865 (1996).

[61] D. M. Ceperley and B. J. Alder, Phys. Rev. Lett. **45**, 566 (1980).

[62] V. I. Anisimov, J. Zaanen, and O. K. Andersen, Phys. Rev. B **44**, 943 (1991).

[63] S. L. Dudarev, G. A. Botton, S. Y. Savrasov, C. J. Humphreys, and A. P. Sutton, Phys. Rev. B **57**, 1505 (1998).

[64] M. T. Paques-Ledent and P. Tarte, Spectrochim. Acta, Part A **30**, 673 (1974).

[65] M. T. Paques-Ledent and P. Tarte, Spectrochim. Acta, Part A **29**, 1007 (1973).

[66] W. Paraguassu, P. T. C. Freire, V. Lemos, S. M. Lala, L. A. Montoro, and J. M. Rosolen, J. Raman Spectrosc. **36**, 213 (2005).

[67] C. M. Burba and R. Frech, J. Electrochem. Soc. **151**, A1032 (2004).

[68] A. Ait-Salah, J. Dodd, A. Mauger, R. Yazami, F. Gendron, and C. M. Julien, Z. Anorg. Allg. Chem. **632**, 1598 (2006).

[69] S. Klotz, J.-C. Chervin, P. Munsch, and G. L. Marchand, J. Phys. D: Appl. Phys. **42**, 075413 (2009).

[70] F. Birch, Phys. Rev. **71**, 809 (1947).

[71] T. Maxisch and G. Ceder, Phys. Rev. B **73**, 174112 (2006).

[72] F. Zhou, M. Cococcioni, C. A. Marianetti, D. Morgan, and G. Ceder, Phys. Rev. B **70**, 235121 (2004).

[73] H. Shi, W. Luo, B. Johansson, and R. Ahuja, Phys. Rev. B **78**, 155119 (2008).

[74] R. D. Shannon and C. T. Prewitt, Acta Crystallogr., Sect. B: Struct. Sci. **25**, 925 (1969).

[75] J. Suntivich, K. J. May, H. A. Gasteiger, J. B. Goodenough, and Y. Shao-Horn, Science **334**, 1383 (2011).

[76] D.-H. Seo, H. Gwon, S.-W. Kim, J. Kim, and K. Kang, Chem. Mater. **22**, 518 (2010).